Boosting Catalytic Combustion of Ethanol by Tuning Morphologies and Exposed Crystal Facets of α-Mn$_2$O$_3$

Wangwang Liu [1], Yong Men [1,2,*], Fei Ji [1], Feng Shi [1], Jinguo Wang [1], Shuang Liu [1], Tamerlan T. Magkoev [3,*] and Wei An [1,*]

1 School of Chemistry and Chemical Engineering, Shanghai University of Engineering Science, Shanghai 201620, China
2 Mechanical Industrial Key Laboratory of Boiler Low-Carbon Technology, Shanghai University of Engineering Science, Shanghai 201620, China
3 Laboratory of Surface Physics and Catalysis, Department of Condensed Matter Physics, North Ossetian State University, Vatutina 44-46, Vladikavkaz 362025, Russia
* Correspondence: men@sues.edu.cn (Y.M.); t_magkoev@mail.ru (T.T.M.); weian@sues.edu.cn (W.A.); Tel.: +86-21-6787-4046 (Y.M. & W.A.); Fax: +86-21-6779-1214 (Y.M. & W.A.)

Abstract: Three types of α-Mn$_2$O$_3$ catalysts with different well-defined morphologies (cubic, truncated octahedra and octahedra) and exposed crystal facets have been successfully prepared via hydrothermal processes, and evaluated for ethanol total oxidation with low ethanol concentration at low temperatures. The α-Mn$_2$O$_3$-cubic catalyst shows a superior catalytic reaction rate than that of α-Mn$_2$O$_3$-truncated octahedra and α-Mn$_2$O$_3$-octahedra under high space velocity of 192,000 mL/(g·h). Based on the characterization results obtained from XRD, BET, FE-SEM, HR-TEM, FT-IR, H$_2$-TPR, XPS, ethanol-TPD, and CO-TPSR techniques, the observed morphology-dependent reactivity of α-Mn$_2$O$_3$ catalysts can be correlated to the good low-temperature reducibility, abundant surface Mn^{4+} and adsorbed reactive oxygen species, which was originated from the exposed (001) crystal planes. Through tuning the morphology and exposed (001) crystal facet of α-Mn$_2$O$_3$, a highly active ethanol oxidation catalyst with high selectivity and excellent stability is obtained. The developed approach may be applied broadly to the development of the design principles for high-performance low-cost and environmentally friendly Mn-based oxidation catalysts.

Keywords: ethanol combustion; manganese oxide; morphology effect; structure-sensitive

1. Introduction

As atmospheric and photochemical contaminants, Volatile Organic Compounds (VOCs) emitted from fossil fuel combustion, transportation, automobile exhaust, and photochemical pollution have caused tremendous detrimental impact on the environment and human's health [1,2]. As one of the typical gaseous pollutants among these VOCs, ethanol derived mainly from the residue of unburned ethanol in ethanol-fueled vehicles [3,4]. By comparing different technologies for burning ethanol into CO$_2$, H$_2$O, and other less hazardous by-products, the catalytic ethanol combustion has been recognized as one of the most viable and environmentally-friendly technologies at low concentration and lower temperature (200–600 °C) owing to its higher efficiency and yields, and lower cost than that of traditional physical/chemical adsorption and non-catalytic thermal oxidation technologies [5]. Thus, the development of the efficient ethanol combustion catalysts is of great significance in reducing ethanol emissions below the limits imposed by the regulation standards.

In the past few decades, noble metal-based catalysts such as Pt, Pd, Ir, Rh and Au [6–10], etc., have been reported to exhibit high performance of ethanol oxidation at low operation temperatures. However, the high cost of noble metals have caused bottlenecked, which limits the economic viability and impedes the widespread use in ethanol-fueled vehicles. Therefore, it is highly desirable to develop an alternative catalyst to substitute for

the noble-metal-based catalyst in order to meet the ever-rigorous ethanol emission standards. Metal oxides, such as Cu/Al_2O_3 [11], CuO/Fe_2O_3 [3], Al/Mn-K [12], $CoFe_2O_4$ [13], Mn-Ce-Zr-O [14], Mn-Cu [15], etc., are considered as the most promising alternative materials, which have been validated via their good catalytic activity, low cost, resistant to poisonings and higher thermal stability. Catalyst composition, specific surface area, crystal and pore structure have been reported to be the key factors in determining the ethanol combustion efficiencies. Despite its excellent catalytic performance, most of the studies were performed to work the catalysts under lower space velocity, remaining insufficient for practical application.

During recent years, more and more researchers have paid their attention to nano/microsized metal oxides material with different morphologies, such as tube, rods, wires, spheres, cubic, and octahedra, etc. Generally, the catalytic reaction performance of catalyst particles can be finely tuned by their anisotropic morphology, which further results in different exposed crystal facets, to this end, the degree of coordination unsaturation of catalytically active atoms are vital for the correlation between structure and catalytic performance, as reported in the earlier literatures [16–22]. For instance, Shen et al. [21] investigated that the catalytic oxidation of CO over nanoscale catalytic particles of Co_3O_4 with controlled size and topology, and found that Co_3O_4 nanorod have highly structure-ordered, constituting 40% of the (110) crystal plane on the nanorod surface was able to oxidize CO at $-77\,^\circ$C, showing a 10 times higher activity than conventional Co_3O_4 catalysts. Trovarelli et al. [19] reported that soot combustion over ceria was a surface-dependent reaction and (100) surface for nanocubes; (100), (110) and partially (111) for nanorods, and enclosed octahedral possessed much higher catalytic performance for soot oxidation than ceria polycrystalline powders, which in agreement with the density functional theory (DFT) calculations that the formation energies of ceria surface oxygen vacancies decreased tendency were obtained: (111) < (100) < (110) [23]. Hence, morphology-controlled synthesis of nano/microsized metal oxides further brings up new opportunities for tuning the catalytic activity, selectivity, and stability of metal oxide catalysts via selectively exposing uniform and higher energy/reactive crystal facets.

For transition-metal oxides (TMOs), the Mars-Van Krevelen (MVK) mechanism is proverbially accepted to be responsible for the oxidation of VOCs; the gas-phase organic molecules are oxidized by the active oxygen species of TMOs, then re-oxidized by gas-phase oxygen molecules, which will regenerate or maintain the oxidation state of the metal cations [24,25]. The MVK mechanism is mainly caused by transition-metal cations which possess the ability of electron transport or lattice oxygen mobility for their d or f outer electrons. As an important TMOs, earth-abundant manganese oxides (MnO_x), such as MnO_2, Mn_2O_3, and Mn_3O_4, are considered as promising catalytic materials due to their potentially high catalytic performance, low cost, low toxicity, and durable for the catalytic oxidation of VOCs [1,26–31], soot [32,33], or CO [34–36]. The superior efficiency catalytic reactivity of MnO_x material mainly related to the existence of various valence states of manganese ions (Mn^{2+}, Mn^{3+}, and Mn^{4+} species) and lattice oxygen on the MnO_x materials, resulting in a facile and reversible Mn^{3+}/Mn^{2+} or Mn^{4+}/Mn^{3+} redox cycle [25,32,37–39]. For example, Gandhe et al. [39] revealed that the total oxidation performance of ethyl acetatethe over cryptomelane type octahedral molecular sieve (OMS-2) material was dependent on the existence of Mn^{4+}/Mn^{3+} type redox couples and facile lattice oxygen on catalysts. Peluso et al. [40] reported that high concentration of Mn^{3+} was beneficial to weakening Mn-O bond and increasing the concentration of active oxygen species, which would enhance catalytic performance of MnO_x in the catalytic oxidation of ethanol. Kim et al. [37] reported that VOCs oxidation over manganese oxides catalysts, including Mn_3O_4, Mn_2O_3 and MnO_2 follows $Mn_3O_4 > Mn_2O_3 > MnO_2$ could be correlated to the surface area and oxygen mobility of samples. Hence, the multiple valence states and surface reactive oxygen species of MnO_x catalysts are the major determining factors for the catalytic activity of VOCs oxidation.

So far, much research efforts have been devoted to further develop high-performance MnO_x catalysts with excellent reactivity and selectivity by tailoring the shape of the catalysts [20,32,41,42]. Feng et al. [43] reported different manganese oxides with distinct morphologies (1D-Mn_3O_4 nanorod, 2D-Mn_3O_4 nanoplate, and 3D-Mn_3O_4 nano-octahedron) were synthesized by hydrothermal treatment. The Mn_3O_4 nanoplate catalyst exhibits a small crystal size, large surface area, more exposed (112) facets, abundant Mn^{4+}, and defective structure, contributing to a superior catalytic performance at the high space velocity of 120,000 mL g^{-1} h^{-1}. Wang et al. [41] reported shape-dependent activation of peroxy monosulfate by single crystal α-Mn_2O_3 (cube, octahedra and truncated octahedra) for catalytic phenol degradation in aqueous solution followed the order of catalytic activity of three α-Mn_2O_3 samples as α-Mn_2O_3-cubic > α-Mn_2O_3-octahedra > α-Mn_2O_3-truncated. Recently, [32] crystal facet-dependent reactivity of α-Mn_2O_3 microcrystalline catalyst for soot combustion was reported, in the rank of α-Mn_2O_3-cubic > α-Mn_2O_3-truncated octahedra > α-Mn_2O_3-octahedra. The origin of the superior performance of cubic α-Mn_2O_3 was correlated with the higher concentration of low-coordinated surface oxygen sites and improved surface redox properties on deliberately exposed (001) crystal facets.

To the best of our knowledge, the ethanol total combustion over different morphologies α-Mn_2O_3 materials with selectively exposed different crystal facets has not yet been investigated in the literature. In the presented work, three types of controllably synthesized three types of α-Mn_2O_3 catalysts with different morphology and exposed crystal facets were prepared by a facile hydrothermal route. The intrinsic properties of α-Mn_2O_3 catalysts are characterized by means of XRD, BET, FE-SEM, HR-TEM, FT-IR, H_2-TPR, XPS, Ethanol-TPD, and CO-TPSR techniques. Kinetic study was also performed to understand the morphology-dependent reactivity of α-Mn_2O_3 catalysts for ethanol total combustion. As demonstrated by various physicochemical characterizations, the morphology of α-Mn_2O_3 catalysts was identified to play a crucial role in exposing the different crystal facets and therefore dictate the catalytic performance of the ethanol total combustion.

2. Results and Discussion

2.1. Crystal Phase Structure and Morphology of Catalysts

The crystal phase of as-prepared manganese oxides catalysts was confirmed by XRD, whose patterns were presented in Figure 1. All catalysts showed the same main characteristic diffraction peaks with a remarkable crystallinity, agreeing well with the previous work [32,41,44,45]. The main characteristic diffraction peaks at 23.1°, 33.0°, 38.2°, 45.2°, 49.3°, 55.2°, and 65.9° (2θ values), corresponding to the (211), (222), (400), (332), (431), (440), and (622) (hkl) planes, can be well-indexed to the body centered cubic phase crystalline structure of α-Mn_2O_3 with the lattice parameter a = 0.9409 nm (JCPDS Card No:00-041-1442). From the diffraction profiles of α-Mn_2O_3-C, α-Mn_2O_3-TO, and α-Mn_2O_3-O, one can observe the considerably sharpening of the characteristic diffraction peaks with the increasing relative intensity, indicating the enhanced crystallinity. The crystalline sizes of α-Mn_2O_3-C, α-Mn_2O_3-TO and α-Mn_2O_3-O were estimated to be 24.8 nm, 51.6 nm and 76.1 nm, respectively. No diffraction peaks of other impurities phase were observed via the XRD patterns, further implying that three catalysts possessed high phase purity.

The morphologies and crystallographic microstructures of α-Mn_2O_3 catalysts were investigated by using FE-SEM and HR-TEM. Figure 2 clearly showed that three catalysts possessed the same Mn_2O_3 crystal phase but presented completely different morphologies, including cubic, truncated octahedra, and octahedra, implying the morphologies can be controlled by adjusting hydrothermal temperatures and different solvents. The observations were quite similar to the previous works [32,41]. The α-Mn_2O_3-C presented well-regulated cubic morphology with amiable edges and particle sizes ranging between 0.7 and 2.0 μm (Figure 2a,b). Based on these FE-SEM images (Figure 2c–f), the α-Mn_2O_3-TO and α-Mn_2O_3-O catalysts clearly presented uniform distribution of truncated octahedra and octahedra morphologies with the smooth surface and sharp edges and particle sizes ranging from 1.0–2.2 μm and 0.8–2.5 μm, respectively. No particle with other morpholo-

gies was observed in the three samples with cubic, truncated octahedra, and octahedra morphologies (Figure 2a,c,e).
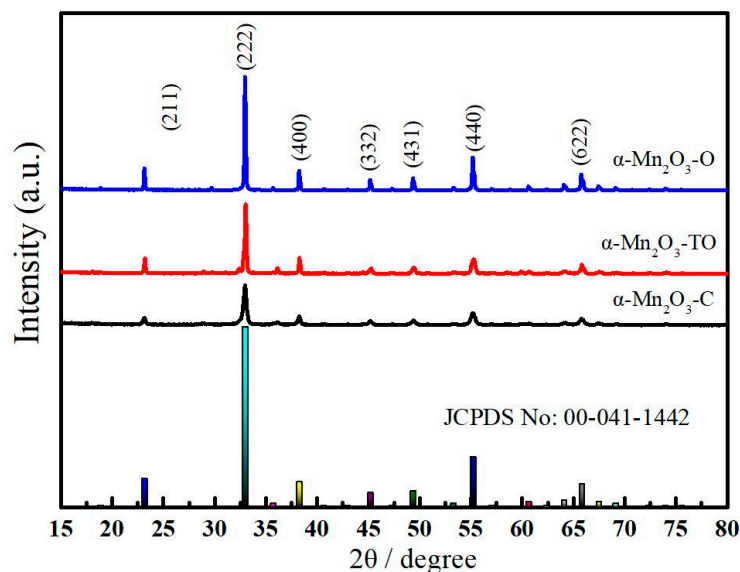

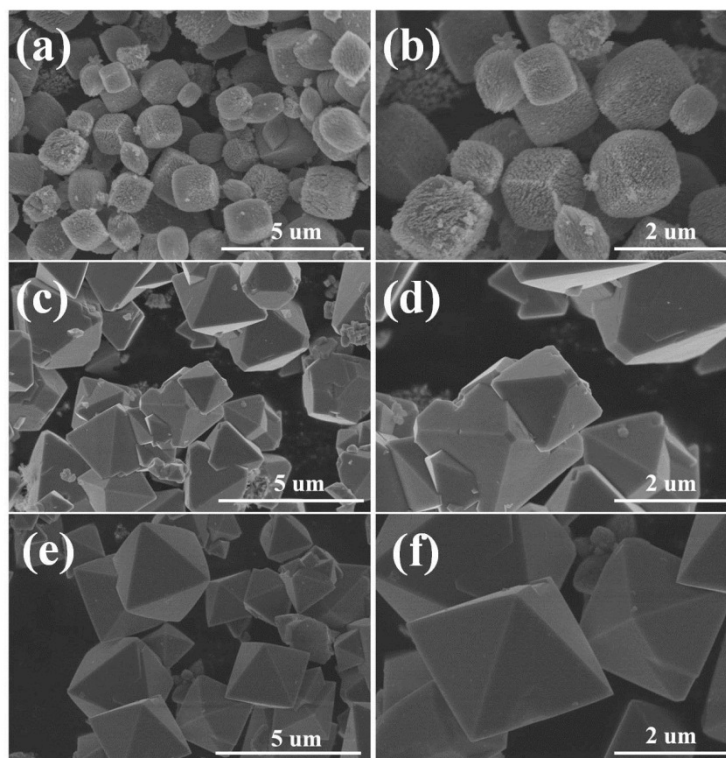**Figure 1.** XRD patterns of α-Mn$_2$O$_3$ catalysts with different morphologies.

Figure 2. FE-SEM images of α-Mn$_2$O$_3$ catalysts with different morphologies. α-Mn$_2$O$_3$-C (**a,b**), α-Mn$_2$O$_3$-TO (**c,d**), α-Mn$_2$O$_3$-O (**e,f**).

TEM characterizations were performed on various α-Mn$_2$O$_3$ catalysts to further investigate the morphologies and crystallographic features i.e., the exposed crystal facets. TEM and HR-TEM images (Figure 3) clearly showed that three α-Mn$_2$O$_3$ catalysts presented morphologies of cubic (Figure 3a), truncated octahedra (Figure 3c), and octahedra (Figure 3e), in consistent with the results of FE-SEM and previous reports [32,41]. Figure 3c showed that the lattice fringe of cubic α-Mn$_2$O$_3$ (004) facets was 0.23 nm, and α-Mn$_2$O$_3$-C mainly exposed the (001) crystal facets as the crystal (001) facets and (004) facets were parallel

to each other. Figure 3f showed that α-Mn$_2$O$_3$-O mainly exposed the crystal (111) facets which stays parallel to the (222) facets. In addition, the truncated octahedra (Figure 3d) exposed truncated crystal (001) facets and crystal (111) facets, in good agreement with the previous works [32,41,44]. According to the literatures [46,47], crystal growth rates in the direction perpendicular to a high-index plane are usually much faster than those along the normal direction of a low-index plane, therefore high-index planes are rapidly eliminated during particle formation. Li et al. [44] studied the influence of preparation conditions on the morphology control of α-Mn$_2$O$_3$ and found out that the domain relied on the different growth rates of [001] and [111] crystallographic directions. Therefore, growing orientation along the [001] and [111] crystallographic directions can form both morphologies of cubic and octahedra with exposed (001) and (111) crystal facets, respectively.
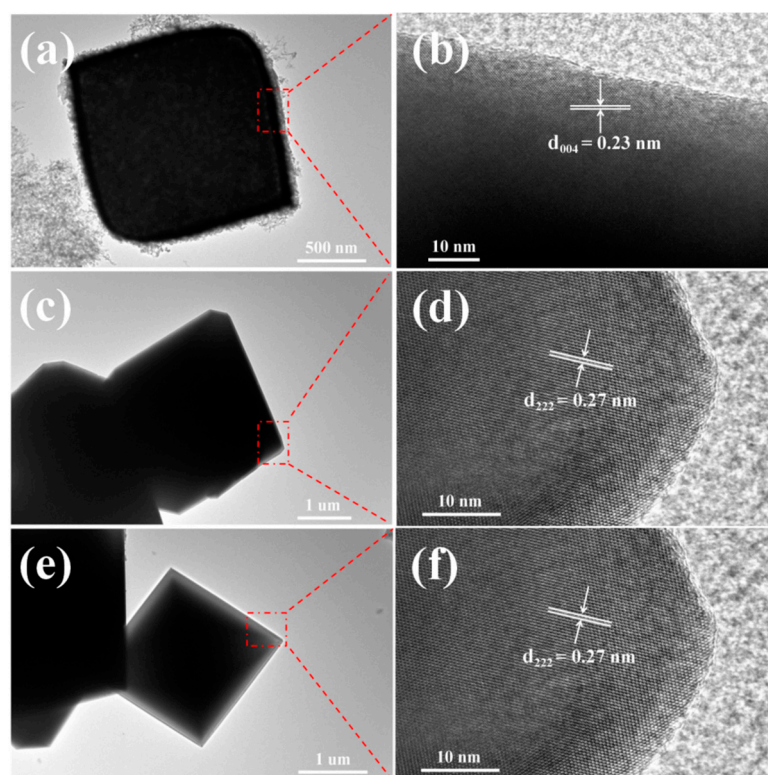

Figure 3. HR-TEM images of α-Mn$_2$O$_3$ catalysts with different morphologies. α-Mn$_2$O$_3$-C (**a**,**b**), α-Mn$_2$O$_3$-TO (**c**,**d**), α-Mn$_2$O$_3$-O (**e**,**f**).

FT-IR spectra of the α-Mn$_2$O$_3$ catalysts with different morphologies were shown in Figure S1. It can be seen that the different catalysts presented the analogical positions of characteristic peaks as in literature [32], which located around 481, 529, 572, 660, 1626, 3432 cm^{-1}, respectively. In the fingerprint region, the presence of peaks at around 529 cm^{-1}, 572 cm^{-1}, and 660 cm^{-1} were assigned to the Mn-O-Mn band asymmetric and symmetric stretching vibration and the peak corresponded to metal-oxygen chains (Mn-O band) bending vibrations in α-Mn$_2$O$_3$ [48]. In the functional group region, the weak broad band at around 3432 cm^{-1} was attributed to the stretching vibration modes of the hydroxyl functional group and the peak at around 1626 cm^{-1} was mainly caused by the adsorbed water molecules on the α-Mn$_2$O$_3$.

2.2. Surface Area and Surface Chemical Properties

The N$_2$ physical adsorption-desorption isotherms and BJH pore-size distribution patterns of different α-Mn$_2$O$_3$ catalysts are shown in Figure S2 and their S$_{BET}$, D$_p$, and V$_p$ are listed in Table 1. All catalysts displayed a similar type IV isotherms, with H3 (P/P$_0$ = 0.6–1.0) hysteresis rings, indicating the presence of microporous and mesoporous

in the α-Mn$_2$O$_3$ materials. Table 1 showed that α-Mn$_2$O$_3$-C, α-Mn$_2$O$_3$-TO, and α-Mn$_2$O$_3$-O catalysts possessed surface area of 30.5, 2.5, and 1.0 m^2/g, the pore diameter of 22.1, 13.5, 12.9 nm, pore volume of 0.212, 0.009, and 0.004 cm^3/g, respectively. Comparing to α-Mn$_2$O$_3$-TO and α-Mn$_2$O$_3$-O catalyst, α-Mn$_2$O$_3$-C had much higher surface area, pore diameter, and pore volume, which is favorable for the activation and diffusion of the reactants, thereby enhancing the catalytic performance of the catalyst. From the adsorption-condition of N$_2$ molecules on the surface of porous material at 77 K, the surface area and pore volume of α-Mn$_2$O$_3$-TO and α-Mn$_2$O$_3$-O catalysts primarily relied on interparticle spaces, thus both catalysts were seen as less developed porous α-Mn$_2$O$_3$ catalysts. The morphologies and structures of catalysts would have great influence on pore size distributions, which is likely to be correlated with the distribution of the active sites [24,49]. From FE-SEM images, one can also observed that all catalysts were composed of solid single crystals with smooth planes, which brought about much smaller surface area, pore diameter, and pore volume.

Table 1. Preparation parameters, BET specific surface areas (S$_{BET}$), pore volumes (V$_P$), Pore diameters (D$_P$), reduction peak temperatures, H$_2$ consumptions and surface element composition of three α-Mn$_2$O$_3$ catalysts.

Catalyst	S$_{BET}$ [a] (m^2/g)	V$_P$ (cm^3/g)	D$_P$ [b] (nm)	T (°C)		H$_2$ Consumptions (mmol/g)			Surface Element Molar Ratio [c]	
				Peak1	Peak2	Mn$_2$O$_3$→Mn$_3$O$_4$	Mn$_3$O$_4$→MnO	Total	Mn^{4+}/Mn^{3+}	O$_{ads}$/O$_{latt}$
α-Mn$_2$O$_3$-C	30.5	0.212	22.1	287	383	2.5	3.7	6.2	1.27	0.53
α-Mn$_2$O$_3$-TO	2.5	0.009	13.5	409	458	3.6	2.5	6.1	1.15	0.43
α-Mn$_2$O$_3$-O	1.0	0.004	12.9	449	496	3.7	2.3	6.0	1.07	0.38

[a] Specific surface areas were calculated by the BET method. [b] The data was calculated via the BJH method according to the N$_2$ adsorption-desorption isotherms. [c] The ratios were calculated based on the peak areas processed by the XPS-Peak software.

The redox properties of various α-Mn$_2$O$_3$ catalysts were examined by using H$_2$-TPR technique. Figure 4 presented the reduction profiles of the α-Mn$_2$O$_3$ catalysts in the temperature range from 100 °C to 600 °C. Two typical peaks can be observed for all catalysts. The different H$_2$-TPR profiles of three α-Mn$_2$O$_3$ samples indicated the different reactivity of reduction of reactive oxygen species in different local environments [50,51]. The α-Mn$_2$O$_3$-O catalyst exhibited a large reduction peak centered at about 496 °C with a low temperature shoulder peak at 449 °C, corresponding to H$_2$ consumptions of 2.3 and 3.7 mmol·g^{-1}, respectively (Table 1). Comparing with α-Mn$_2$O$_3$-O catalyst with exposed crystal (111) facets, a similar reduction pattern was observed for the α-Mn$_2$O$_3$-TO catalyst with exposed (001) & (111) crystal facets, which had the primary reduction peak at 458 °C and the low temperature shoulder peak n at 409 °C, corresponding to H$_2$ consumptions of 3.6 and 2.5 mmol·g^{-1}, respectively (Table 1). The alteration of the reduction behavior might be caused by the presence of crystal (001) facets on truncated octahedra α-Mn$_2$O$_3$ sample. In the case of α-Mn$_2$O$_3$-C catalyst, two distinct lower temperature reduction peaks at 287 and 383 °C were observed, corresponding to H$_2$ consumptions of 2.5 and 3.7 mmol·g^{-1}, respectively (Table 1). The two reduction peaks of various α-Mn$_2$O$_3$ samples corresponds to a stepwise transformation under H$_2$ atmosphere. The first step peak represented the reduction of Mn$_2$O$_3$ to Mn$_3$O$_4$, whereas the second step peak corresponded to the reduction of Mn$_3$O$_4$ to the final state MnO, similar to the findings reported in the previous literatures [27,32,52–56]. The order of low-temperature reducibility for surface oxygen is α-Mn$_2$O$_3$-C with crystal (001) facets > α-Mn$_2$O$_3$-TO with crystal (001) & (111) facets > α-Mn$_2$O$_3$-O with crystal (111) facets, which is related to the fact that surface O atoms on (001) facet, due to its high flexibility, are energetically more facile for release and participation than those on (111) facet [32], suggesting a more facile surface oxygen reducibility for α-Mn$_2$O$_3$-C and morphology-dependence of redox behavior. The excellent reducibility of the α-Mn$_2$O$_3$ could be beneficial to the enhanced catalytic activity for the ethanol combustion.
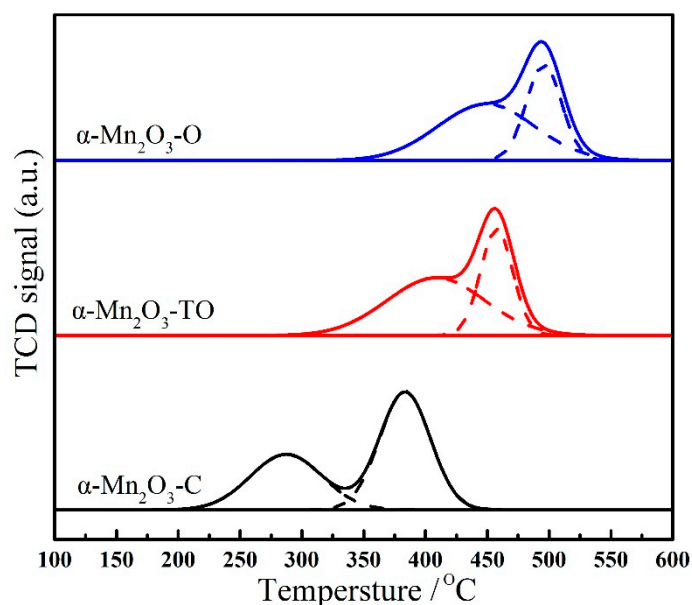
Figure 4. H_2-TPR profiles of α-Mn_2O_3 catalysts with different morphologies.

XPS measurements were carried out to identify the surface element compositions, element valence states, and adsorbed oxygen species of α-Mn_2O_3 catalysts. In the XPS survey spectrum presented in Figure S3A, the peaks of carbon (C 1s), oxygen (O 1s), and manganese (Mn 2p) can be clearly detected. In Figure S3B, the binding energy (BE) obtain at 284.6 eV and 287.8 eV obtained were assigned to the C-C (nonoxygenated carbon) and C-O (oxidized carbon) species, respectively. Figure 5 displayed the Mn 2p and O1s spectra for different samples, respectively. The related results of surface element compositions in molar ratio were listed in Table 1. The XPS spectra of Mn 2p presented two contributions, assignable to spin-orbit splitting into Mn $2p_{3/2}$ (641.6 eV) and Mn $2p_{1/2}$ (653.2 eV), respectively. The BE separation between the two main peaks was 11.6 eV [57]. The Mn 2p spectrum of each catalyst could be further resolved into four peak components, attributable to the presence of surface Mn^{3+} species at BE = 641.2 and 652.9 eV and Mn^{4+} species at BE = 642.6 and 654.0 eV [58]. According to Table 1, the surface Mn^{4+}/Mn^{3+} molar ratio of α-Mn_2O_3-C was significantly higher than the other two catalysts, indicating that α-Mn_2O_3-C with (001) crystal facets possessed more surface Mn^{4+} species. The differences in surface Mn^{4+}/Mn^{3+} molar ratios of three catalysts may be explained by the difference in morphologies and the degree of coordination unsaturation of surface active atoms on exposed crystal facets.

As revealed in Figure 5B, the O1s spectra of different α-Mn_2O_3 catalysts were decomposed into two components at BE = 529.6 and 531.2 eV, corresponding to the surface lattice oxygen (O_{latt}: O^{2-}) and O_{ads} such as O^-, O_2^-, O_2^{2-} and OH^- [37,58–60], respectively. The surface O_{ads}/O_{latt} molar ratios of α-Mn_2O_3-C, α-Mn_2O_3-TO, and α-Mn_2O_3-O were 0.53, 0.43, and 0.38, respectively (Table 1). Obviously, the amount of surface adsorbed oxygen in α-Mn_2O_3-C with (001) facets is much higher than that of α-Mn_2O_3-TO with (111) & (001) and α-Mn_2O_3-O with (111) facets, implying the important role of exposed (001) crystal facet in oxygen vacancy formation. The increase in surface adsorbed oxygen species might have a significant effect in enhancing catalytic performance for total oxidation reactions mainly because the surface oxygen species had higher mobility than lattice oxygen in the presence of abundant oxygen vacancies [61–63].

Oxygen vacancy concentration is crucial in combustion reaction, and oxygen can be chemisorbed on the site of oxygen vacancy to become adsorbed reactive species under reaction atomosphere. Russo et al. [59] have directly detected the existence of oxygen vacancy by Raman characterization, agreeing with the XPS characterization results of surface adsorbed oxygen species.
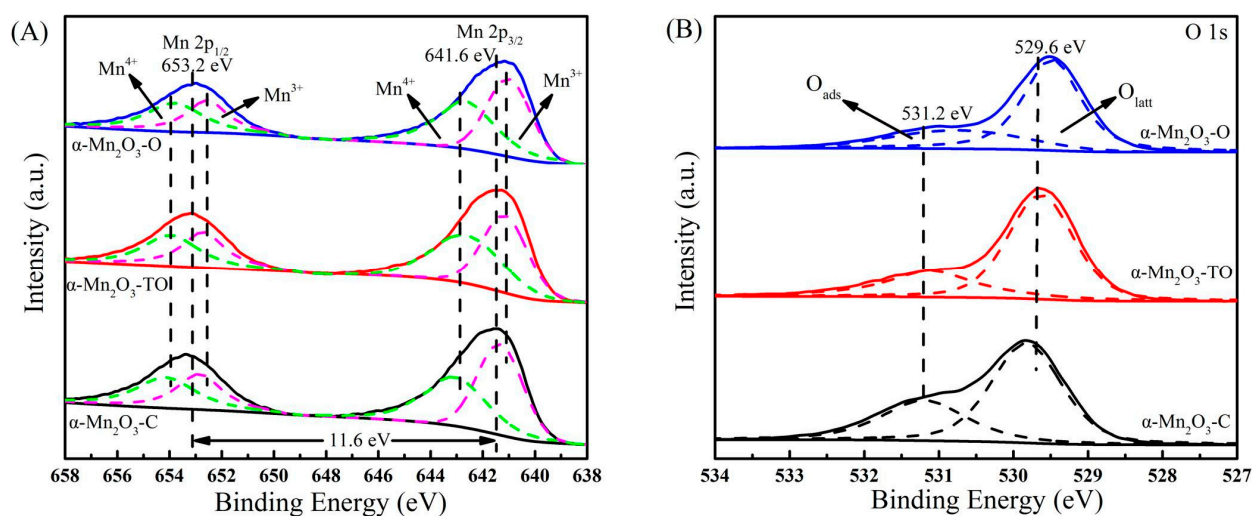
Figure 5. XPS patterns of the Mn 2p (**A**) and O 1s (**B**) of α-Mn_2O_3 catalysts with different morphologies.

In order to further unravel the origin of the morphology effect of α-Mn_2O_3, CO-TPSR was also performed by using CO as probe molecule over online MS. The curves of the CO_2 ($m/z = 44$) signals for three catalysts were displayed in Figure 6. The positions of CO_2 peaks can be related to the different reactivity of the surface reactive oxygen species to oxidize CO. Figure 6 clearly showed the different capability for CO_2 generation by surface active oxygen species over the samples, which was ranked as the decreased order of α-Mn_2O_3-C with (001) facets > α-Mn_2O_3-TO with (001) & (111) facets > α-Mn_2O_3-O with (111) facets. It was evident that theα-Mn_2O_3-C sample with exposed (001) could afford the much more abundant surface reactive oxygen species for CO_2 generation than the other two samples with exposed (111) and mixed (001) & (111) facets, agreeing well with the sequence of the H_2-TPR and XPS results discussed above. The results demonstrated the α-Mn_2O_3-C with (001) facets contains more lattice oxygen and surface oxygen species as activated oxygen species for CO oxidation than (111) facets.
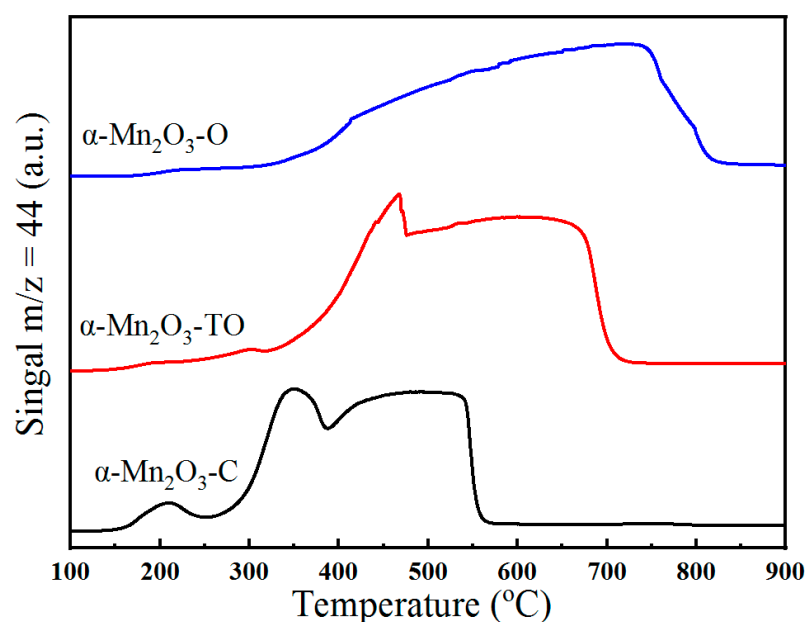

Figure 6. Morphology-dependent CO-TPSR profiles of α-Mn_2O_3 catalysts.

H_2-TPR and CO-TPSR have provided a great deal of practical information on the reactivity of surface oxygen species towards hydrogen molecule. However, the information is indirect as to how strongly the surface and lattice oxygen held in α-Mn_2O_3 catalysts

reacts with substrate molecule i.e., ethanol. Ethanol-TPD is a much more direct measure for the determination of surface oxygen species as compared to H_2-TPR. Hence, the catalytic nature of surface adsorbed reactive oxygen species and the desorption behavior of ethanol on the morphology-controlled α-Mn_2O_3 catalysts with different exposed crystallographic facets has been investigated by using ethanol-TPD technique. Figure 7 showed the ethanol-TPD profiles of different morphologies α-Mn_2O_3 catalysts. As the desorption temperature rises, the ethanol reactant as well as some important intermediates including ethanol, acetaldehyde, CO_2, and H_2O were detected on mass spectrometer, corresponding to the signals of $m/z = 31$, $m/z = 29$, $m/z = 44$, and $m/z = 18$, respectively. It was noticed that the dehydrogenation of ethanol occurred already over three samples in the low temperature range of 40–200 °C, as evidenced by the characteristic peak of acetaldehyde at $m/z = 29$. TPD profiles for α-Mn_2O_3 catalysts show an apparent morphology-dependent CO_2 desorption profile at temperature above 160 °C. The significantly higher intensity as well as the lowered desorption temperature of CO_2 over α-Mn_2O_3-C catalyst strongly suggest that the preferential exposure of (001) crystal facet by tailoring the catalyst morphology may favor the generation of more abundant surface oxygen reactive species and therefore facilitate CO_2 production.
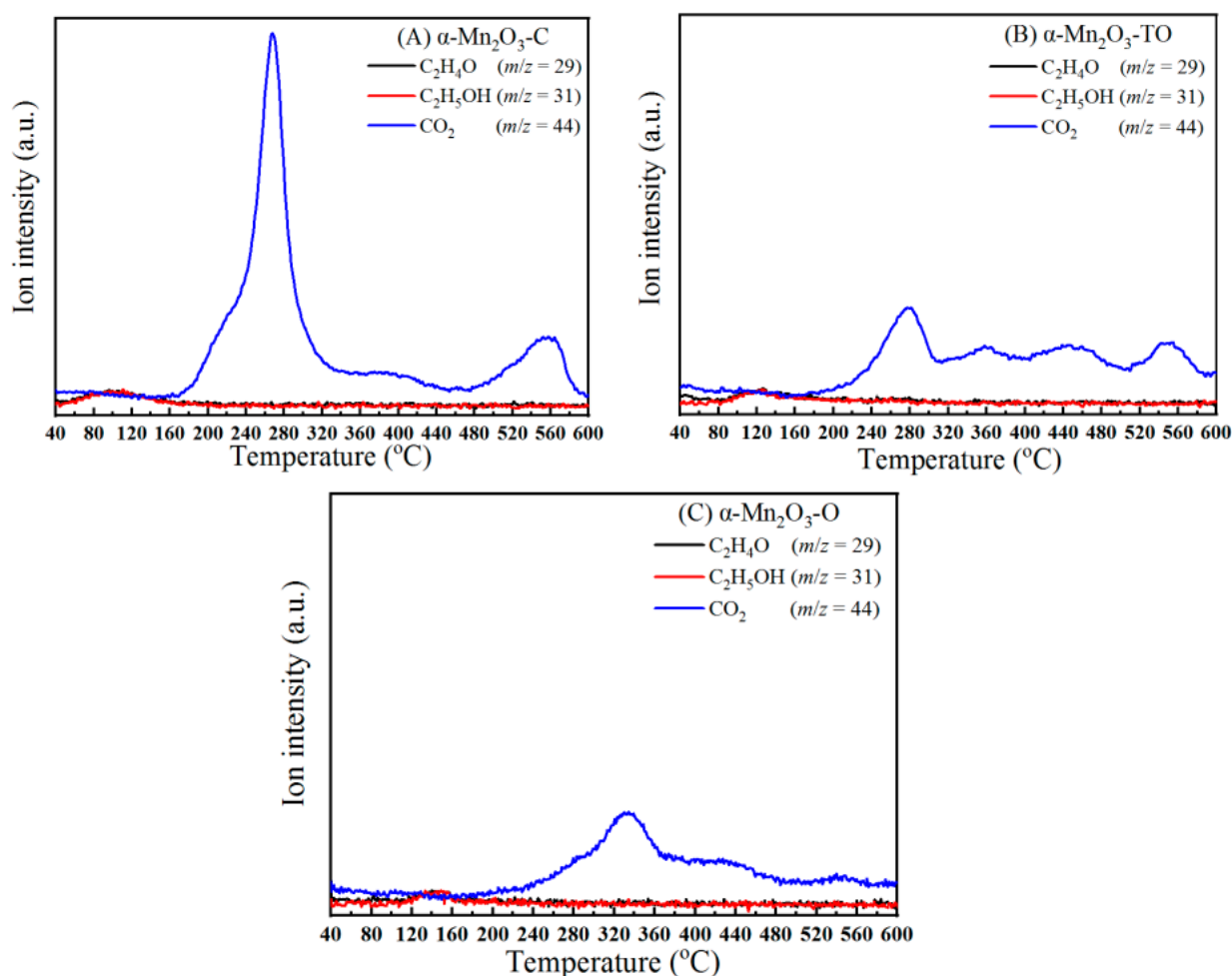

Figure 7. Morphology-dependent ethanol-TPD profiles of α-Mn_2O_3 catalysts: α-Mn_2O_3-C (**A**), α-Mn_2O_3-TO (**B**), α-Mn_2O_3-O (**C**).

2.3. Catalytic Performance of Different Shaped α-Mn_2O_3 Catalysts

The morphology-dependent catalytic performances of α-Mn_2O_3-C, α-Mn_2O_3-TO, and α-Mn_2O_3-O catalysts were evaluated for ethanol total combustion and the results were shown in Figure 8, Figure S4 and Table 2. Figure 8A shows a clear morphology-dependent

catalytic performance for ethanol total combustion with the following order: α-Mn_2O_3-C (190 °C) > α-Mn_2O_3-TO (290 °C) > α-Mn_2O_3-O (340 °C). α-Mn_2O_3-C catalyst with exposed (001) facets exhibited the best catalytic performance on ethanol total oxidation, achieving the complete conversion temperature at 190 °C, which was 150 °C lower than α-Mn_2O_3-O catalyst with exposed crystal (111) facets. The same order of CO_2 yield was found in Figure 8B, exhibiting nearly 100% CO_2 yield at temperature of 240 °C over α-Mn_2O_3-C, 350 °C over α-Mn_2O_3-TO, and 400 °C over α-Mn_2O_3-O catalysts, respectively. Figure 8C showed the volcano-like plot of the acetaldehyde yield over three catalysts, presenting the maximum in acetaldehyde yield of 35.4% at 160 °C over α-Mn_2O_3-C, 45.8% at 230 °C over α-Mn_2O_3-TO, and 42.2% at 300 °C over α-Mn_2O_3-O catalyst, respectively, strongly suggesting that acetaldehyde is the primary intermediate species during ethanol total oxidation, in good accordance with previous work [5,25,28]. It was worth noting that acetaldehyde and CO_2 were the only detected carbon-containing products. On the basis of product distribution observed, we concluded that the cascade reaction pathway of ethanol total combustion via acetaldehyde as important intermediate over different crystal facets of α-Mn_2O_3. Figure 8D and Table 2 further listed the important catalytic data of different α-Mn_2O_3 catalysts with different exposed crystal facets in terms of T_{10}, T_{50}, and T_{90}, which were defined as the values of the reaction temperature corresponding to the ethanol conversions of 10%, 50%, and 90%, respectively. In this study, T_{10} for α-Mn_2O_3-C, α-Mn_2O_3-TO, and α-Mn_2O_3-O catalysts were 90, 151, and 179 °C; T_{50} were 140, 208, and 261 °C; and T_{90} were 178, 259, and 314 °C, respectively. In addition, the normalized ethanol combustion rate of α-Mn_2O_3-C, α-Mn_2O_3-TO, and α-Mn_2O_3-O at 90 °C were about 2.84, 1.53, and 0.84 mmol·min^{-1}·m^{-2}·10^4, respectively. The superior ethanol combustion activity for α-Mn_2O_3-C catalyst with exposed (001) crystal facets than α-Mn_2O_3 with only (111) crystal facets can be closely related to the low-temperature reducibility and highly active surface mobile oxygen species over the α-Mn_2O_3 surface.
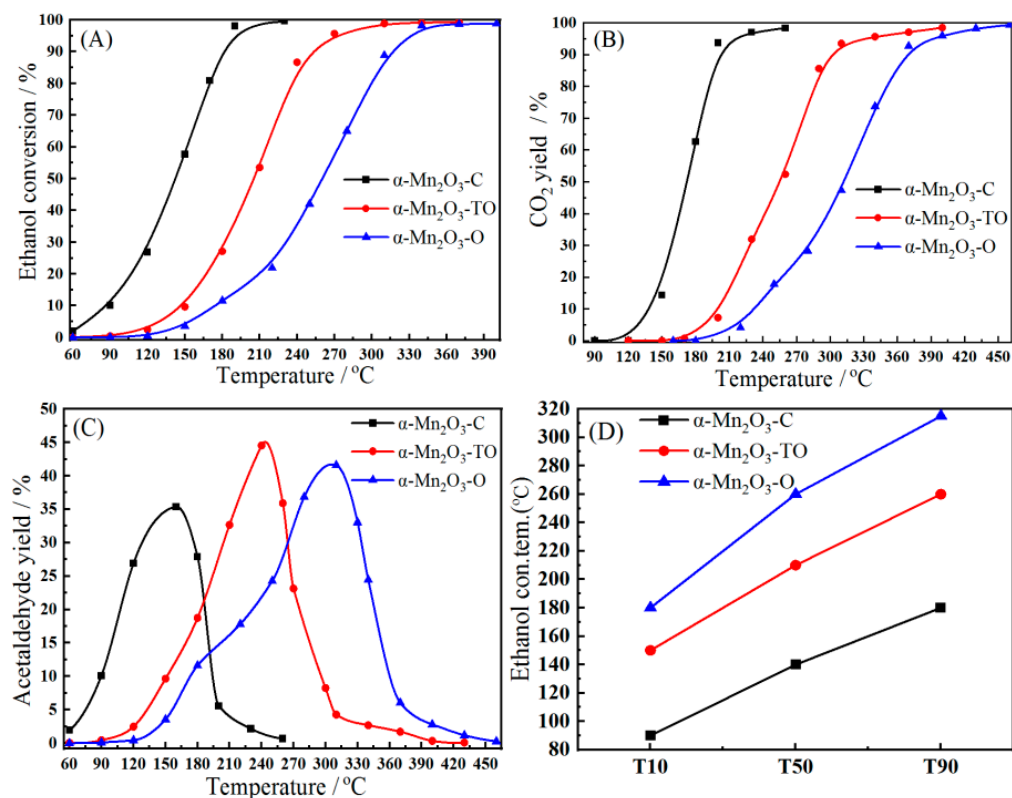

Figure 8. Ethanol conversion (**A**), CO_2 yield (**B**), and acetaldehyde yield (**C**) of ethanol catalytic performance over α-Mn_2O_3 catalysts with different morphologies. (**D**) T10, T50, and T90: defined as the temperature approaching 10%, 50%, and 90%, ethanol conversion with the same space velocity over the three catalysts.

Table 2. The catalytic activity data of the α-Mn$_2$O$_3$ catalysts with different exposed crystal facets for ethanol oxidation under the same reaction conditions: 600 ppm ethanol, 20 vol.% O$_2$, N$_2$ as balance gas, SV = 192,000 mL/(g·h).

Catalysts	Catalytic Activity (°C)			T (°C)	Ethanol Conversion (%)	Normalized Rate (mmol·min^{-1}·m^{-2}) $\times 10^4$	E$_a$ (kJ/mol)	R^2 for E$_a$
	T$_{10}$	T$_{50}$	T$_{90}$					
α-Mn$_2$O$_3$-C	90	140	178	90	10.1	2.84	55.3	0.99
α-Mn$_2$O$_3$-TO	151	208	259	90	0.50	1.53	63.7	0.99
α-Mn$_2$O$_3$-O	179	261	314	90	0.10	0.84	68.3	0.98

The BET surface area is an important parameter in determining the catalytic performance of heterogeneous catalysts [64–66]. Herein, to eliminate the effect of the BET surface areas, the kinetics of ethanol catalytic oxidation were investigated. And Arrhenius plots were obtained over α-Mn$_2$O$_3$ catalysts with different exposed crystal facets in the kinetically controlled regime. The apparent activation energy (E$_a$) was calculated via Arrhenius equation by normalizing reaction rate on per unit BET surface area. The results in Figure 9A and Table 2, showed that α-Mn$_2$O$_3$-C catalyst exhibited the much higher initial normalized ethanol reaction rate at low temperature compared with α-Mn$_2$O$_3$-TO, and α-Mn$_2$O$_3$-O catalysts, in the reverse order of the apparent reaction activation energy. The lower the E$_a$ values indicate the easier oxidation of ethanol, and hence the better performance of a catalyst [1,31,32,34,67]. Under the same reaction conditions, (Table 2) the E$_a$ values of α-Mn$_2$O$_3$-C, α-Mn$_2$O$_3$-TO, and α-Mn$_2$O$_3$-O catalysts were 55.3 kJ/mol, 66.7 kJ/mol, and 68.3 kJ/mol, respectively. The observed morphology effect of α-Mn$_2$O$_3$ on the catalytic activity is presumably related to the nature of exposed crystal facets, and density of surface Mn^{4+} and surface reactive oxygen species, which are responsible for the adsorption/activation of ethanol and oxygen molecules. Hence, α-Mn$_2$O$_3$-C exhibited superior catalytic performance than α-Mn$_2$O$_3$-TO and α-Mn$_2$O$_3$-O catalysts, and further illustrated cubic with (001) facets was more active followed by octahedra with (111) facets, in consistent with our XPS, CO-TPSR, and ethanol-TPD results discussed earlier.
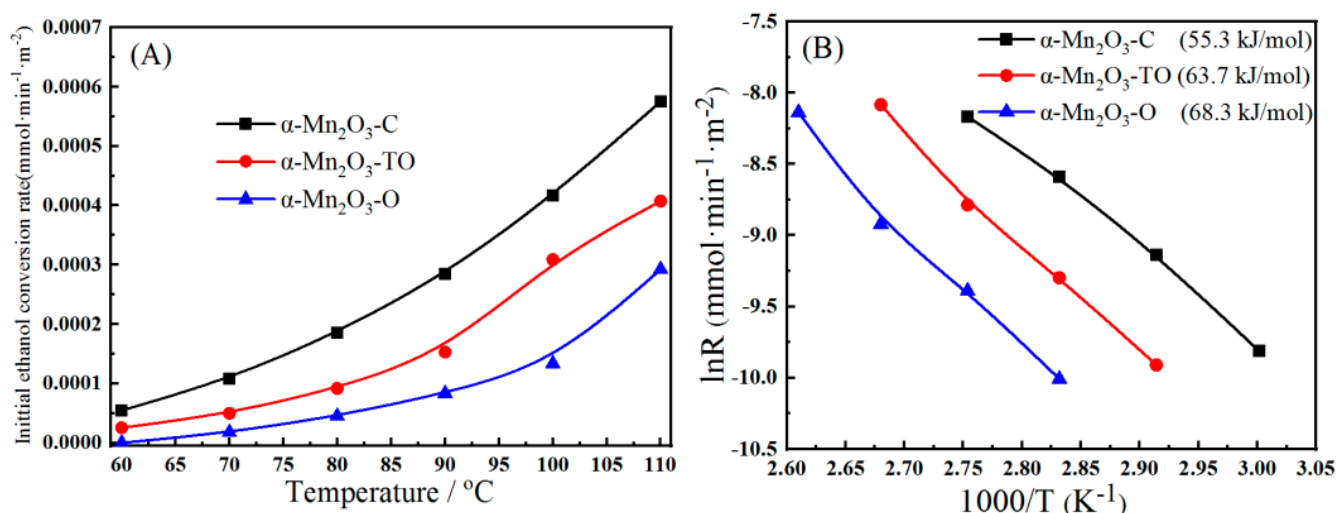

Figure 9. Initial ethanol conversion rates (**A**) and Arrhenius plots in ethanol oxidation (**B**) of α-Mn$_2$O$_3$ catalysts with different morphologies.

As documented in the literature, the dissociation of oxygen molecules on can be seen as the first elementary step of catalytic oxidation over metal or oxide surfaces. Therefore, the activation capability of oxygen molecules play an important role in surfaces of oxidation catalyst. For metal oxide catalyst, oxygen molecules can be facilely adsorbed and activated in the presence of oxygen vacancies, forming surface adsorbed reactive oxygen species, which would participate in the oxidation of organic substrates. Recently, a combined experimental/theoretical study has been performed by our group [32] to investigate the

morphology–dependent reactivity of α-Mn_2O_3 on soot combustion and gained the origin of the difference on their crystal facet-dependent reactivity. The density functional theory (DFT) calculations revealed that the oxygen atoms on top-layer of crystal (001) facets on α-Mn_2O_3 catalysts can flexibly move with the oxygen atoms of sub-layer. By contrary, such a transfer is energetically unfavorable over the crystal (111) facets of α-Mn_2O_3. Moreover, the formation energy of oxygen vacancy over (001) crystal facet and the coordination number (CN) of surface oxygen atoms is remarkably lower than that on (111) surface. As pointed by An et al. [68], the enhanced coordination unsaturation on specially exposed crystal facet may facilitate oxidation reactions. Accordingly, abundant surface Mn^{4+} ions and surface adsorbed reactive oxygen species over (001) surface of α-Mn_2O_3 catalysts may facilitate ethanol/oxygen activation at low temperature and boost ethanol combustion efficiency, in good accordance with our activity and characterization results.

2.4. Effects of SV, Ethanol, and Water Vapor Concentration

The influence of SV, ethanol, and water vapor concentration was investigated over the so-far best-performing α-Mn_2O_3-C catalysts and presented in Figure 10. The effect of SV in Figure 10A showed that the catalytic performance increased as the SV decreased, and the temperatures for complete ethanol oxidation to CO_2 also shifted from 230 °C down to 180 °C. The temperature values corresponding to the maximum acetaldehyde yield also decreased from 160 °C to 150 °C, indicating that the activity of the sample increased as the space velocity decreased. The influence of the initial concentration of ethanol was studied and depicted in Figure 10B. Under the reaction conditions of initial ethanol concentration = 1200 ppm, α-Mn_2O_3-C catalyst showed the catalytic activity of T_{10} = 99 °C, T_{50} = 156 °C, and T_{90}= 203 °C which was inferior to those (T_{10} = 90 °C, T_{50} = 140 °C, and T_{90} = 178 °C) obtained from the initial ethanol concentration = 600 ppm as shown in Table 3 and Figure 10B. The impact of steam was also investigated over α-Mn_2O_3-C catalyst. Figure 10C clearly showed that the oxidation rate of ethanol could be considerably suppressed by the presence of steam in the feed, in accordance with the inhibition effect of steam on VOCs combustion in the literatures [28,30,69]. This is not unexpected because the strong and competitive adsorption of water vapor on the catalyst surface may lead to a decrease in the available active sites towards VOCs and oxygen, and therefore inhibit ethanol combustion reaction. Under the reaction conditions of 6 vol.% H_2O in the feed, the catalytic activity (T_{10} = 150 °C, T_{50} = 195 °C, and T_{90} = 218 °C) over α-Mn_2O_3-C catalyst became much worse than that under conditions without H_2O (T_{10} = 90 °C, T_{50} = 140 °C, and T_{90} = 178 °C), as shown in Table 3 and Figure 10D.

2.5. The Stability of α-Mn_2O_3-C Catalyst

Figure 11 displayed the ethanol catalytic combustion performance as a function of time on stream over the best-performing α-Mn_2O_3-C catalyst with exposed (001) crystal facets under the conditions of reaction temperature 230 °C, SV 192,000 mL/(g·h), and feed composition of 600 ppm ethanol, 20 vol.% O_2, 6 vol.% H_2O, N_2 as balance gas. Apparently, with the addition of 6 vol.% H_2O, the α-Mn_2O_3-C catalyst exhibited outstanding reaction stability for ethanol oxidation was assessed with experiments lasting at over 230 °C. According to the stability data of successive measurements (Figure 11A), the ethanol conversion, acetaldehyde yield, and CO_2 yield remained almost unchanged for the test duration of more than 50 h, illustrating the excellent stability over the entire run of the stability test. Figure 11B presented almost the same XRD diffraction peaks on the used α-Mn_2O_3-C catalyst as the pattern on the fresh example. Furthermore, the FE-SEM inset in Figure 11B illustrated that the α-Mn_2O_3-C sample remained their original cubic morphology after the test duration of more than 50 h. Based on the stability test, it appeared that α-Mn_2O_3-C could be used as one of the promising manganese based catalysts for efficient ethanol combustion under practical conditions.
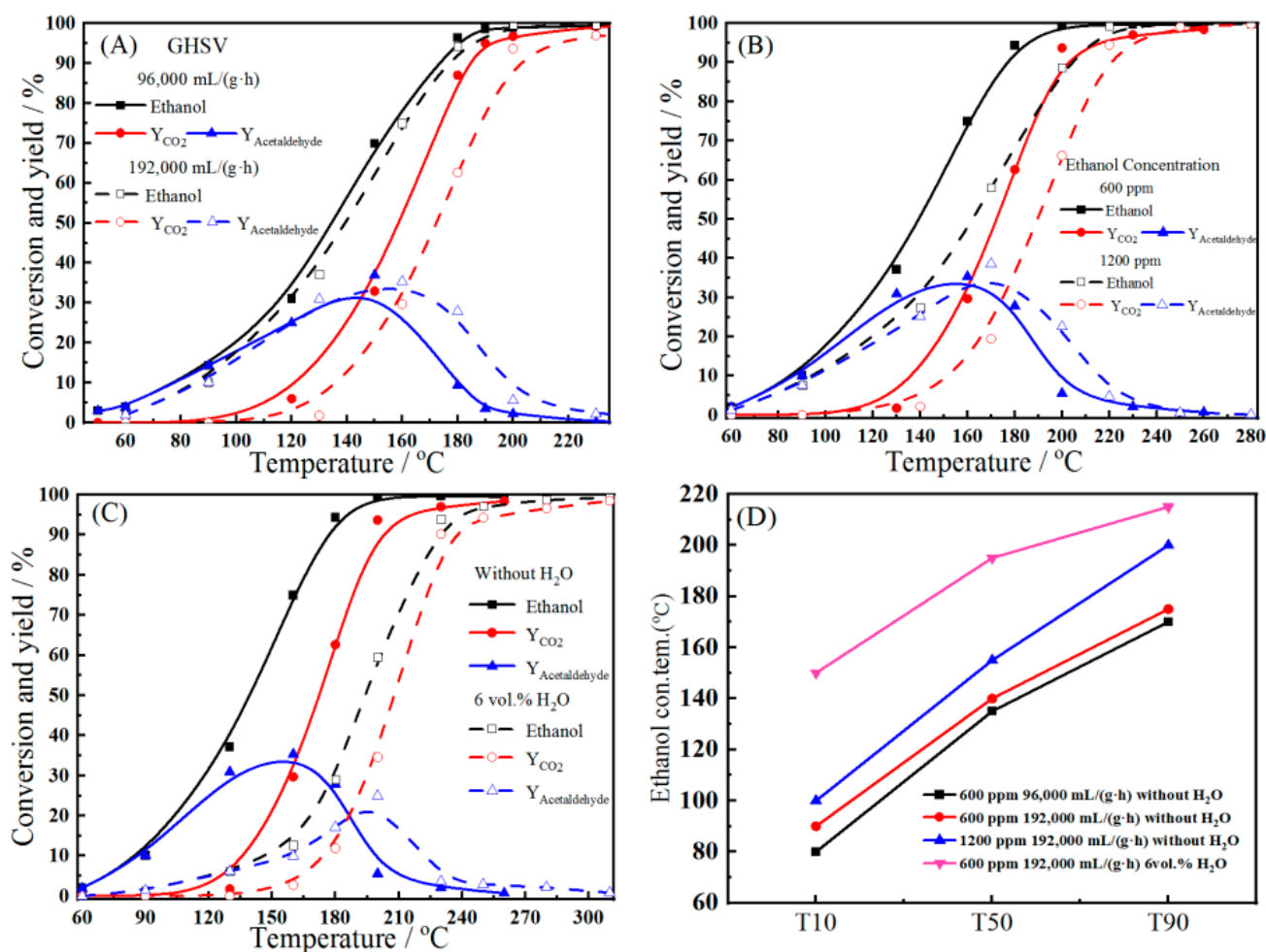
Figure 10. The catalytic performances of the α-Mn_2O_3-C catalyst under different reaction conditions of ethanol combustion, the effect of performance for (**A**) space velocity: 96,000 mL/(g·h) and 192,000 mL/(g·h). (**B**) ethanol concentration: 600 ppm and 1200 ppm. (**C**) steam: 6 vol.% H_2O. (**D**) T10, T50, and T90: the temperature over the α-Mn_2O_3-C catalyst with different conditions where ethanol conversion approaches 10%, 50%, and 90%, respectively.
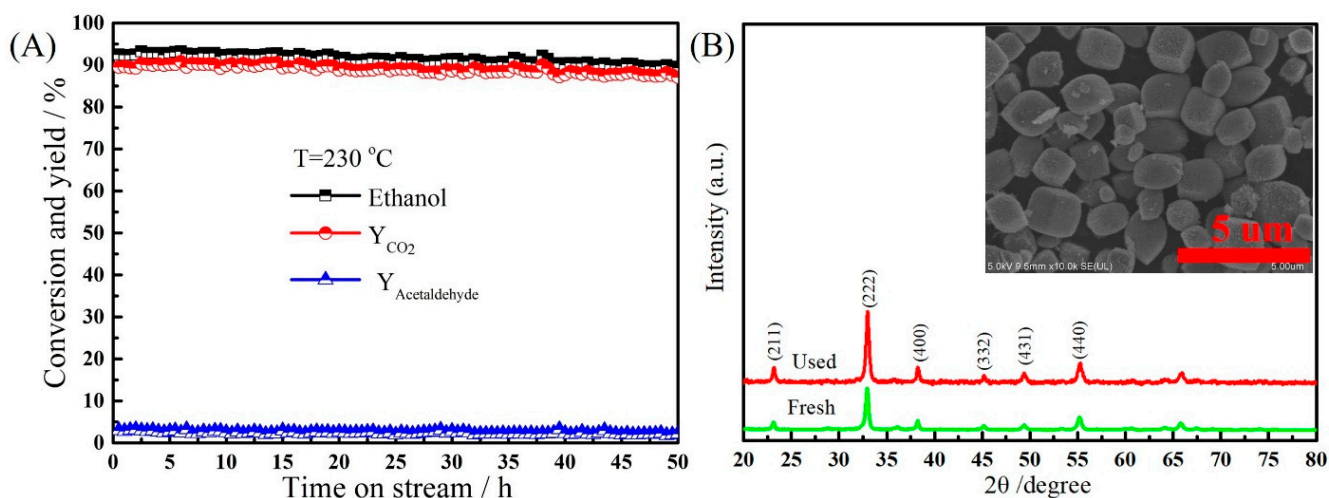

Figure 11. (**A**) The stability test of the α-Mn_2O_3-C catalyst for ethanol total combustion. (**B**) XRD patterns of used and fresh α-Mn_2O_3-C catalysts, FE-SEM image of used α-Mn_2O_3-C catalyst. Reaction conditions: reaction temperature 230 °C, 6 vol.% H_2O, ethanol concentration 600 ppm, 20 vol.% O_2, N_2 balance, SV = 192,000 mL/(g·h).

Table 3. The catalytic performances of the α-Mn$_2$O$_3$-C catalyst under different reaction conditions of ethanol oxidation.

Ethanol Con. Tem (°C)	600 ppm Ethanol SV of 96,000 mL/(g·h)	600 ppm Ethanol SV of 192,000 mL/(g·h)	1200 ppm Ethanol SV of 192,000 mL/(g·h)	600 ppm Ethanol, 6 vol.% H$_2$O, SV of 192,000 mL/(g·h)
T$_{10}$	79	90	99	150
T$_{50}$	136	140	156	195
T$_{90}$	172	178	203	218

3. Materials and Methods

3.1. Catalyst Synthesis

Three types of morphology-tuned α-Mn$_2$O$_3$ catalysts, including morphology of cubic, truncated octahedra and octahedra, were synthesized via a low-temperature hydrothermal method according to the literatures earlier [32,41,44,45]. For truncated octahedra and octahedra α-Mn$_2$O$_3$ catalysts was prepared by solvothermal method with different solvents. The first catalyst α-Mn$_2$O$_3$-octahedra (refer as α-Mn$_2$O$_3$-O), for a typical synthesis, Mn(NO$_3$)$_2$·4H$_2$O (16 mmol) was dissolved in ethanol (52 mL) at room temperature (RT) under vigorous magnetic stirring for 20 min to form a homogeneous solution, which then then transferred to a 60 mL Teflon-lined stainless-steel autoclave. The autoclave was tightly sealed and heated for 10 h at 383 K. After hydrothermal reaction, the autoclave was cooled down to RT naturally. The resulting solid product was centrifuged, washed three times in distilled water and ethanol to eliminate impurity ions, and then placed into an oven at 373 K overnight to obtain the α-Mn$_2$O$_3$-O catalyst. Similarly, the synthetic method of the second catalyst, α-Mn$_2$O$_3$-truncated octahedra (referred to as α-Mn$_2$O$_3$-TO), merely changed the solvent replaced by 2-butanol. All catalysts should be calcined in air atmosphere for 2 h at 873 K. The third catalyst, α-Mn$_2$O$_3$-cubic (refer as α-Mn$_2$O$_3$-C), glucose (6 mmol) was added into a KMnO$_4$ solution (6 mmol of KMnO$_4$ was dissolved in 60 mL of distilled water) at RT under vigorous magnetic stirring for another 20 min to form a homogeneous solution, which then was transferred to a 100 mL autoclave, which was tightly sealed and heated for 10 h at 433 K, after natural cooling to RT, immediately followed via centrifugation, washing, and final drying to obtain the precursor MnCO$_3$. Prior to yielding cubic α-Mn$_2$O$_3$ catalyst, the precursor MnCO$_3$ should be calcined in air atmosphere for 2 h at 873 K with a ramp rate of 5 K/min. Finally, a series of α-Mn$_2$O$_3$ catalysts were crushed and sieved to 40–60 mesh for catalytic activity tests.

3.2. Catalyst Characterization

The crystalline structure of catalysts was recorded by the powder X-ray diffraction (XRD) on a Bruker D2 Phaser (Bruker Axs Gmbh, Karlsruhe, Germany) using Cu-Kα radiation. The 2θ of the XRD range from 15° to 80° with the scan speed during analysis was 0.5 s/step. Field emission-scanning electron microscopy (FE-SEM) surface morphology of the catalyst on Hitachi S-4800 instrument (Hitachi, Ibaraki, Japan). High-resolution transmission electron microscopy (HR-TEM) images of the catalysts were taken on Hitachi JMF-2100 instrument (Hitachi, Japan). The Fourier transform infrared (FT-IR) spectrum of the catalyst was collected by using a Nicolet 380 spectrometer (Nicolet, Madison, WI, USA) in the range of 400–4000 cm^{-1}. The nitrogen adsorption−desorption isotherms were performed on a Micromeritics ASAP 2460 (Micromeritics, Norcross, GA, USA) analyzer at 77 K. By using Brunauer-Emmet-Teller (BET) and Barrett-Joyner-Halenda (BJH) models, specific surface areas (S$_{BET}$), pore diameter (D$_P$) and pore volume (V$_P$) of the catalysts were calculated from the adsorption branches of the isotherms. Prior to measurement it was degassed at least for 5 h at 393 K. The X-ray photoelectron spectroscopy (XPS) measurements of the catalyst was examined on ESCALAB 250 Xi (Thermo Fisher Scientific, Waltham, MA, USA) using Al-Kα X-ray source. The binding energy scale was corrected for surface charging by use of the C 1s peak of contaminant carbon as reference at 284.6 eV.

Hydrogen temperature-programmed reduction (H$_2$-TPR) measurements were carried out on a chemisorption analyzer (Micromeritics, Auto Chem II2920, Norcross, GA, USA)

instrument, which was equipped with a thermal conductivity detector (TCD) to calibrate the H_2 consumption of metal valence reduction. Before H_2-TPR experiments started, the catalysts (50 mg, 40–60 mesh) were loaded into a U-shaped fixed-bed quartz micro-reactor and pretreated in an Ar atmosphere of 50 mL/min for 1 h at 573 K, and then cooled down to 373 K. The pretreated catalysts were reduced under a mixture-gas of 10 vol.% H_2–90 vol.% Ar flow with 30 mL/min and heated in the range of 373 K to 1173 K with a ramp rate of 10 k/min. Ethanol temperature-programmed desorption (Ethanol-TPD) measurements were carried out via using a Micromeritics AutoChem II2920 instrument connected to mass spectrometry (MS) (Hiden, HPR20, Warrington, UK) instrument. The catalysts (50 mg, 40–60 mesh) were loaded into a U-shaped fixed-bed quartz micro-reactor and previously treated for 0.5 h at 373 K in pure He flow with 30 mL/min, cooling down to 313 K. The adsorption experiment of ethanol was carried out with a He flow of 30 mL/min. After saturation, the temperature was increased from 313 K to 873 K with a ramping rate of 10 K/min. The desorption substances coming from α-Mn_2O_3 catalysts were monitored by means of online MS apparatus.

3.3. Temperature-Programmed Surface Reactions (TPSR) and Mixed-Gas without Oxygen

The CO-TPSR measurements(Micromeritics, Auto Chem II2920, America) to characterize the nature of the active sites of catalysts on α-Mn_2O_3 catalysts were performed in a fixed-bed tubular quartz system (Φ = 6.0 mm) via using MS, where masses (m/e: CO = 28, CO_2 = 44) were monitored. 50 mg of each catalyst were previously treated for 0.5 h at 773 K in a pure Ar flow of 50 mL/min, in order to remove physical adsorption oxygen, cooling down to 373 K. The mixture-gas of 5 vol.% CO-95 vol.% He with a total flow rate of 30 mL/min increasing the temperature from 373 K to 1173 K, and a ramping rate of 5 K/min.

3.4. Catalytic Performance Evaluation

The morphology-dependent catalytic performance of three α-Mn_2O_3 catalysts for ethanol total combustion were evaluated in a flow-through quartz micro-reactor (Φ = 6.0 mm), which was positioned in the center of the tube furnace at atmospheric pressure. The catalytic combustion temperature was monitored via a thermocouple, which was placed in a few millimeters above the bottom of the catalyst fixed-bed. 100 mg (40–60 mesh) of catalyst was held in place by using quartz wool at upper and lower ends [70,71]. The total flow rate of the uniformity mixed-gas (600 ppm ethanol/20 vol.% O_2/N_2 balance gas) passed through the catalyst fixed-bed remained at 320 mL/min, which was detected by using mass flow-meter. The space velocity (SV) of catalytic ethanol combustion was 192,000 mL/(g × h). Prior to catalytic evaluation, to exclude the effect of impurities, the catalysts should be pretreated for 30 min at 333 K in air atmosphere. The outflow gases of the oxidation reaction from the reactor were quantitatively analyzed online via a Gas Chromatograph (Shimadzu, GC-2014C, Kyoto, Japan) which was equipped with two detectors of a thermal conductivity detector (TCD) and a flame ionization detector (FID). And TCD was only responsible for the detection of CO_2, FID responsible for the detection of ethanol and acetaldehyde due to it can respond to almost all organic matter. In the present work, the final products of ethanol total combustion were CO_2 and H_2O. During the ethanol oxidation, the main products were acetaldehyde, CO_2 and other remaining trace products which can be ignored. The effect of performance for SV, ethanol and water vapor concentration were explored. The thermal stability of α-Mn_2O_3 catalyst was tested for 50 h under the condition of 6.5 mg catalyst was diluted with 100 mg of SiO_2, 600 ppm ethanol, 6vol.% H_2O, 20 vol.% O_2, N_2 as the equilibrium gas, and SV was 192,000 mL/(g × h). The conversion of ethanol was calculated based on the participation of ethanol as follows (1):

$$X = \left(\left(C_{\text{acetaldehyde out}} + \tfrac{C_{co_2 \text{ out}}}{2} \right) \middle/ \left(C_{\text{acetaldehyde out}} + \tfrac{C_{co_2 \text{ out}}}{2} + C_{\text{ethanol out}} \right) \right) \times 100\%$$

$$S_{co_2} = \left(\tfrac{C_{co_2 \text{ out}}}{2} \middle/ \left(C_{\text{acetaldehyde out}} + \tfrac{C_{co_2 \text{ out}}}{2} + C_{\text{ethanol out}} \right) \right) \times 100\%$$

$$S_{\text{acetaldehyde}} = C_{\text{acetaldehyde out}} \middle/ \left(C_{\text{acetaldehyde out}} + \left(\tfrac{C_{co_2 \text{ out}}}{2} \right) \right) \times 100\%$$

$$Y_{\text{yield}} = \text{conversion} \times \text{selectivity} \times 100\%, \tag{1}$$

where X, ethanol conversion rate; C, concentration; S, selectivity of products; Y, yield of products.

3.5. Kinetic Analysis for Ethanol Total Oxidation

To obtain kinetics data, the kinetic research was performed under ethanol conversion below 15% with the condition of 600 ppm ethanol, 20 vol.%O_2, N_2 as the equilibrium gas, and SV was 192,000 mL/(g·h) for three α-Mn_2O_3 catalysts in the range of 333 K to 383 K. The catalytic activation energy (E_a) of the catalysts were calculated according to the Arrhenius Equation (2):

$$\ln R = -A \, \exp\left(-\frac{E_a}{RT}\right), \tag{2}$$

where E_a, apparent activation energy (kJ/mol); R, the reaction rate (mol·min^{-1}·m^{-2}); T, the value of the reaction temperature (K).

4. Conclusions

In summary, a series of α-Mn_2O_3 catalysts with different morphologies, including cubic, truncated octahedra and octahedra, were controllably synthesized by using a facile hydrothermal process and systematically investigated for their morphology-dependent catalytic performance in ethanol total combustion. The catalytic activity according to each manganese oxide catalyst was in the order of α-Mn_2O_3-C > α-Mn_2O_3-TO > α-Mn_2O_3-O. The present study indicated that this morphology-dependent reactivity of α-Mn_2O_3 nanocrystal was originated from the chemical nature of the exposed (001) facets. As revealed by characterization results of HR-TEM, H_2-TPR, XPS, CO-TPSR, ethanol-TPD, the superior activity of α-Mn_2O_3-C sample can be well correlated with its enhanced low temperature reducibility, abundant surface Mn^{4+} species and surface reactive oxygen species governed by the specially exposed (001) facets. Moerover, the effect of space velocity and feed compsotion (ethanol and steam) were also investigated on α-Mn_2O_3-C catalyst under different reaction conditions. Furthermore, the α-Mn_2O_3-C catalyst exhibited good stability for 50 h at 230 °C in the presence of 6 vol.% H_2O, demonstrating that α-Mn_2O_3-C catalyst could be used as promising catalyst for effecnt practical total oxidation of ethanol. This study presents a new strategy to design and develop the catalyst for efficient combustion of ethanol by morphological control of earth-abundant inexpensive Mn-based catalysts.

Author Contributions: Conceptualization, Y.M. and W.A.; methodology, Y.M.; software, W.L.; validation, W.L., F.J. and Y.M.; formal analysis, W.L., F.J. and J.W.; investigation, W.L.; resources, Y.M.; data curation, W.L., F.S. and S.L.; writing—original draft preparation, W.L., Y.M., W.A. and T.T.M.; writing—review and editing, W.L., W.A., T.T.M. and Y.M.; supervision, Y.M. and T.T.M.; project administration, Y.M.; funding acquisition, Y.M. All authors have read and agreed to the published version of the manuscript.

Data Availability Statement: The data presented in this study are available on request from the corresponding author.

Conflicts of Interest: The authors declare no conflict of interest.

References

1. Si, W.Z.; Wang, Y.; Peng, Y.; Li, X.; Li, K.Z.; Li, J.H. A high-efficiency gamma-MnO_2-like catalyst in toluene combustion. *Chem. Commun.* **2015**, *51*, 14977–14980. [CrossRef] [PubMed]
2. Benrabaa, R.; Benadda, A.; Hammiche-Bellal, Y.; Boukhlouf, H.; Trentesaux, M.; Rubbens, A.; Vannier, R.N.; Lofberg, A. Characterization and catalytic properties of Ni-Fe spinel catalysts for total oxidation of ethanol. *ChemistrySelect* **2019**, *4*, 6415–6420. [CrossRef]
3. Litt, G.; Almquist, C. An investigation of CuO/Fe_2O_3 catalysts for the gas-phase oxidation of ethanol. *Appl. Catal. B Environ.* **2009**, *90*, 10–17. [CrossRef]
4. Rintramee, K.; Fottinger, K.; Rupprechter, G.; Wittayakun, J. Ethanol adsorption and oxidation on bimetallic catalysts containing platinum and base metal oxide supported on MCM-41. *Appl. Catal. B Environ.* **2012**, *115*, 225–235. [CrossRef]
5. Aguero, F.N.; Barbero, B.P.; Gambaro, L.; Cadús, L.E. Catalytic combustion of volatile organic compounds in binary mixtures over MnO_x/Al_2O_3 catalyst. *Appl. Catal. B Environ.* **2009**, *91*, 108–112. [CrossRef]
6. Avgouropoulos, G.; Oikonomopoulos, E.; Kanistras, D.; Ioannides, T. Complete oxidation of ethanol over alkali-promoted Pt/Al_2O_3 catalysts. *Appl. Catal. B Environ.* **2006**, *65*, 62–69. [CrossRef]
7. Zhang, S.; Guo, Y.Y.; Li, X.Y.; Wu, X.; Li, Z. The double peaks and symmetric path phenomena in the catalytic activity of Pd/Al_2O_3-TiO_2 catalysts with different TiO_2 contents. *J. Solid State Chem.* **2018**, *262*, 335–342. [CrossRef]
8. Gan, Y.H.; Tong, Y.; Jiang, Z.W.; Chen, X.W.; Li, H.G.; Jiang, X. Electro-spraying and catalytic combustion characteristics of ethanol in meso-scale combustors with steel and platinum meshes. *Energy Convers. Manag.* **2018**, *164*, 410–416. [CrossRef]
9. Santos, V.P.; Carabineiro, S.A.C.; Tavares, P.B.; Pereira, M.F.R.; Órfão, J.J.M.; Figueiredo, J.L. Oxidation of CO, ethanol and toluene over TiO_2 supported noble metal catalysts. *Appl. Catal. B Environ.* **2010**, *99*, 198–205. [CrossRef]
10. Tan, T.H.; Scott, J.; Ng, Y.H.; Taylor, R.A.; Aguey-Zinsou, K.F.; Amal, R. Understanding plasmon and band gap photoexcitation effects on the thermal-catalytic oxidation of ethanol by TiO_2-supported gold. *ACS Catal.* **2016**, *6*, 1870–1879. [CrossRef]
11. Wahlberg, A.; Pettersson, L.J.; Bruce, K.; Andersson, M.; Jansson, K. Preparation, evaluation and characterization of copper catalysts for ethanol fuelled diesel engines. *Appl. Catal. B Environ.* **1999**, *23*, 271–281. [CrossRef]
12. Peluso, M.A.; Pronsato, E.; Sambeth, J.E.; Thomas, H.J.; Busca, G. Catalytic combustion of ethanol on pure and alumina supported K-Mn oxides: An IR and flow reactor study. *Appl. Catal. B Environ.* **2008**, *78*, 73–79. [CrossRef]
13. Hammiche-Bellal, Y.; Benadda, A.; Meddour-Boukhobza, L.; Barama, S.; Djadoun, A.; Barama, A. Preparation and catalytic activity in ethanol combustion reaction of cobalt-iron spinel catalysts. *Catal. Commun.* **2013**, *42*, 62–67. [CrossRef]
14. Rao, T.; Shen, M.; Jia, L.; Hao, J.; Wang, J. Oxidation of ethanol over Mn–Ce–O and Mn–Ce–Zr–O complex compounds synthesized by sol–gel method. *Catal. Commun.* **2007**, *8*, 1743–1747. [CrossRef]
15. Morales, M.R.; Barbero, B.P.; Cadús, L. Total oxidation of ethanol and propane over Mn-Cu mixed oxide catalysts. *Appl. Catal. B Environ.* **2006**, *67*, 229–236. [CrossRef]
16. Hu, L.; Peng, Q.; Li, Y. Selective synthesis of Co_3O_4 nanocrystal with different shape and crystal plane effect on catalytic property for methane combustion. *J. Am. Chem. Soc.* **2008**, *130*, 16136–16137. [CrossRef] [PubMed]
17. Li, Y.; Shen, W.J. Morphology-dependent nanocatalysts: Rod-shaped oxides. *Chem. Soc. Rev.* **2014**, *43*, 1543–1574. [CrossRef]
18. Wang, F.; Dai, H.X.; Deng, J.G.; Bai, G.M.; Ji, K.M.; Liu, Y.X. Manganese oxides with rod-, wire-, tube-, and flower-Like morphologies: Highly effective catalysts for the removal of toluene. *Environ. Sci. Technol.* **2012**, *46*, 4034–4041. [CrossRef]
19. Aneggi, E.; Wiater, D.; de Leitenburg, C.; Llorca, J.; Trovarelli, A. Shape-Dependent activity of ceria in soot combustion. *ACS Catal.* **2014**, *4*, 172–181. [CrossRef]
20. Dai, Y.T.; Men, Y.; Wang, J.G.; Liu, S.; Li, S.; Li, Y.Y.; Wang, K. Tailoring the morphology and crystal facet of Mn_3O_4 for highly efficient catalytic combustion of ethanol. *Colloids Surf. A Physicochem. Eng. Asp.* **2021**, *627*, 121276. [CrossRef]
21. Xie, X.; Yong, L.; Liu, Z.Q.; Haruta, M.; Shen, W. Low-temperature oxidation of CO catalysed by Co_3O_4 nanorods. *Nature* **2009**, *458*, 746–749. [CrossRef] [PubMed]
22. Yin, J.Z.; Yu, Z.N.; Gao, F.; Wang, J.J.; Pang, H.A.; Lu, Q.Y. Low-symmetry iron oxide nanocrystals bound by high-index facets. *Angew. Chem. Int. Ed.* **2010**, *49*, 6328–6332. [CrossRef] [PubMed]

23. Nolan, M.; Parker, S.C.; Watson, G.W. The electronic structure of oxygen vacancy defects at the low index surfaces of ceria. *Surf. Sci.* **2005**, *595*, 223–232. [CrossRef]

24. Qu, Z.P.; Bu, Y.B.; Qin, Y.; Wang, Y.; Fu, Q. The improved reactivity of manganese catalysts by Ag in catalytic oxidation of toluene. *Appl. Catal. B Environ.* **2013**, *132*, 353–362. [CrossRef]

25. Santos, V.P.; Pereira, M.F.R.; Orfao, J.J.M.; Figueiredo, J.L. The role of lattice oxygen on the activity of manganese oxides towards the oxidation of volatile organic compounds. *Appl. Catal. B Environ.* **2010**, *99*, 353–363. [CrossRef]

26. Vaculikova, L.; Valovicova, V.; Plevova, A.E.; Napruszewska, B.D.; Duraczynska, D.; Karcz, R.; Serwicka, E.M. Synthesis, characterization and catalytic activity of cryptomelane/montmorillonite composites. *Appl. Clay Sci.* **2021**, *202*, 8065–8068. [CrossRef]

27. Tang, W.X.; Wu, X.F.; Li, D.Y.; Wang, Z.; Liu, G.; Liu, H.D.; Chen, Y.F. Oxalate route for promoting activity of manganese oxide catalysts in total VOCs' oxidation: Effect of calcination temperature and preparation method. *J. Mater. Chem. A* **2014**, *2*, 2544–2554. [CrossRef]

28. Bai, B.Y.; Li, J.H.; Hao, J.M. 1D-MnO$_2$, 2D-MnO$_2$ and 3D-MnO$_2$ for low-temperature oxidation of ethanol. *Appl. Catal. B Environ.* **2015**, *164*, 241–250. [CrossRef]

29. Li, X.; Zheng, J.K.; Liu, S.; Zhu, T.L. A novel wormhole-like mesoporous hybrid MnCoO$_x$ catalyst for improved ethanol catalytic oxidation. *J. Colloid. Interface Sci.* **2019**, *555*, 667–675. [CrossRef]

30. Lahousse, C.; Bernier, A.; Grange, P.; Delmon, B.; Papaefthimiou, P.; Ioannides, T.; Verykios, X. Evaluation of γ-MnO$_2$ as a VOC removal catalyst: Comparison with a noble metal catalyst. *J. Catal.* **1998**, *178*, 214–225. [CrossRef]

31. Liu, Y.X.; Dai, H.X.; Deng, J.G.; Du, Y.C.; Li, X.W.; Zhao, Z.X.; Wang, Y.; Gao, B.Z.; Yang, H.G.; Guo, G.S. In situ poly(methyl methacrylate)-templating generation and excellent catalytic performance of MnO$_x$/3DOM LaMnO$_3$ for the combustion of toluene and methanol. *Appl. Catal. B Environ.* **2013**, *140*, 493–505. [CrossRef]

32. Cheng, L.; Men, Y.; Wang, J.; Wang, H.; An, W.; Wang, Y.; Duan, Z.; Liu, J. Crystal facet-dependent reactivity of α-Mn$_2$O$_3$ microcrystalline catalyst for soot combustion. *Appl. Catal. B Environ.* **2017**, *204*, 374–384. [CrossRef]

33. Ji, F.; Men, Y.; Wang, J.G.; Sun, Y.L.; Wang, Z.D.; Zhao, B.; Tao, X.T.; Xu, G.J. Promoting diesel soot combustion efficiency by tailoring the shapes and crystal facets of nanoscale Mn$_3$O$_4$. *Appl. Catal. B Environ.* **2019**, *242*, 227–237. [CrossRef]

34. Xu, J.; Deng, Y.Q.; Luo, Y.; Mao, W.; Yang, X.J.; Han, Y.F. Operando Raman spectroscopy and kinetic study of low-temperature CO oxidation on an α-Mn$_2$O$_3$ nanocatalyst. *J. Catal.* **2013**, *300*, 225–234. [CrossRef]

35. Ghiassee, M.; Rezaei, M.; Meshkani, F.; Mobini, S. Preparation of the Mn/Co mixed oxide catalysts for low-temperature CO oxidation reaction. *Environ. Sci. Pollut. Res.* **2021**, *28*, 379–388. [CrossRef] [PubMed]

36. Rezaei, P.; Rezaei, M.; Meshkani, F. Ultrasound-assisted hydrothermal method for the preparation of the M-Fe$_2$O$_3$-CuO (M: Mn, Ag, Co) mixed oxides nanocatalysts for low-temperature CO oxidation. *Ultrason. Sonochem.* **2019**, *57*, 212–222. [CrossRef]

37. Kim, S.C.; Shim, W.G. Catalytic combustion of VOCs over a series of manganese oxide catalysts. *Appl. Catal. B Environ.* **2010**, *98*, 180–185. [CrossRef]

38. Mitran, G.; Chen, S.J.; Seo, D.K. Role of oxygen vacancies and Mn^{4+}/Mn^{3+} ratio in oxidation and dry reforming over cobalt-manganese spinel oxides. *Mol. Catal.* **2020**, *483*, 110704. [CrossRef]

39. Gandhe, A.R.; Rebello, J.S.; Figueiredo, J.L.; Fernandes, J.B. Manganese oxide OMS-2 as an effective catalyst for total oxidation of ethyl acetate. *Appl. Catal. B Environ.* **2007**, *72*, 129–135. [CrossRef]

40. Peluso, M.A.; Gambaro, L.A.; Pronsato, E.; Gazzoli, D.; Thomas, H.J.; Sambeth, J.E. Synthesis and catalytic activity of manganese dioxide (type OMS-2) for the abatement of oxygenated VOCs. *Catal. Today* **2008**, *133*, 487–492. [CrossRef]

41. Saputra, E.; Muhammad, S.; Sun, H.; Ang, H.M.; Tadé, M.; Wang, S. Shape-controlled activation of peroxymonosulfate by single crystal α-Mn$_2$O$_3$ for catalytic phenol degradation in aqueous solution. *Appl. Catal. B Environ.* **2014**, *154–155*, 246–251. [CrossRef]

42. Li, S.; Men, Y.; Liu, S.; Wang, J.G. Boosting the efficiencies of ethanol total combustion by Cs incorporation into rod-shaped alpha-MnO$_2$ catalysts. *Colloids Surf. A Physicochem. Eng. Asp.* **2022**, *650*, 129607. [CrossRef]

43. Feng, B.B.; Qin, C.L.; Shi, Y.; Zhang, L.D. Catalytic combustion study of ethanol over manganese oxides with different morphologies. *Energy Fuels* **2022**, *36*, 9221–9229. [CrossRef]

44. Li, W.N.; Zhang, L.; Sithambaram, S.; Yuan, J.; Shen, X.F.; Aindow, M.; Suib, S.L. Shape evolution of single-crystalline Mn$_2$O$_3$ using a solvothermal approach. *J. Phys. Chem. C* **2007**, *111*, 14694–14697. [CrossRef]

45. Lei, S.; Tang, K.; Zhen, F.; Liu, Q.; Zheng, H. Preparation of α-Mn$_2$O$_3$ and MnO from thermal decomposition of MnCO$_3$ and control of morphology. *Mater. Lett.* **2006**, *60*, 53–56. [CrossRef]

46. Wang, D.; Dai, H. Low-Temperature synthesis of single-crystal germanium nanowires by chemical vapor deposition. *Angew. Chem. Int. Ed.* **2002**, *41*, 4977–4980. [CrossRef]

47. Han, N.; Zhou, Z.Y.; Sun, S.G.; Ding, Y.; Wang, Z.L. Synthesis of tetrahexahedral platinum nanocrystals with high-index facets and high electro-oxidation activity. *Science* **2007**, *316*, 732–735.

48. Chen, Z.W.; Jiao, Z.; Pan, D.Y.; Li, Z.; Wu, M.H.; Shek, C.H.; Wu, C.M.L.; Lai, J.K.L. Recent advances in manganese oxide nanocrystals: Fabrication, characterization, and microstructure. *Chem. Rev.* **2012**, *112*, 3833–3855. [CrossRef]

49. Zhang, L.; Qin, Z.; Liu, Z.; Hou, X.; Yi, L. Novel Mn$_3$O$_4$ micro-octahedra: Promising cataluminescence sensing material for acetone. *Chem. Mater.* **2009**, *41*, 5066–5071. [CrossRef]

50. Gac, W. The influence of silver on the structural, redox and catalytic properties of the cryptomelane-type manganese oxides in the low-temperature CO oxidation reaction. *Appl. Catal. B Environ.* **2007**, *75*, 107–117. [CrossRef]

51. Hua, J.L.; Gong, S.H.; Tana; Zhang, X.J.; Wei, L.; Wen, J.S. Morphological impact of manganese–cerium oxides on ethanol oxidation. *Catal. Sci. Technol.* **2011**, *1*, 1677–1682.

52. Kapteijn, F.; Singoredjo, L.; Andreini, A.; Moulijn, J.A. Activity and selectivity of pure manganese oxides in the selective catalytic reduction of nitric oxide with ammonia. *Appl. Catal. B Environ.* **1994**, *3*, 173–189. [CrossRef]

53. Han, Y.F.; Chen, F.; Zhong, Z.; Ramesh, K.; Widjaja, E. Controlled synthesis, characterization, and catalytic properties of Mn_2O_3 and Mn_3O_4 nanoparticles supported on mesoporous silica SBA-15. *J. Phys. Chem. B* **2006**, *110*, 24450–24456. [CrossRef] [PubMed]

54. Morales, M.R.; Barbero, B.P.; Cadús, L. Combustion of volatile organic compounds on manganese iron or nickel mixed oxide catalysts. *Appl. Catal. B Environ.* **2007**, *74*, 1–10. [CrossRef]

55. Trawczyński, J.; Bielak, B.; Miśta, W. Oxidation of ethanol over supported manganese catalysts—Effect of the carrier. *Appl. Catal. B Environ.* **2005**, *55*, 277–285. [CrossRef]

56. Strohmeier, B.R.; Hercules, D.M. Surface spectroscopic characterization of manganese/aluminum oxide catalysts. *J. Phys. Chem.* **1984**, *88*, 4922–4929. [CrossRef]

57. Cheng, C.M.; Huang, Y.; Wang, N.; Jiang, T.; Hu, S.; Zheng, B.Z.; Yuan, H.Y.; Xiao, D. Facile fabrication of Mn_2O_3 nanoparticle-assembled hierarchical hollow spheres and their sensing for hydrogen peroxide. *ACS Appl. Mater. Interfaces.* **2015**, *7*, 9526–9533. [CrossRef]

58. Dai, Y.; Wang, X.Y.; Dai, Q.G.; Li, D. Effect of Ce and La on the structure and activity of MnO_x catalyst in catalytic combustion of chlorobenzene. *Appl. Catal. B Environ.* **2012**, *111*, 141–149. [CrossRef]

59. Piumetti, M.; Bensaid, S.; Fino, D.; Russo, N. Nanostructured ceria-zirconia catalysts for CO oxidation: Study on surface properties and reactivity. *Appl. Catal. B Environ.* **2016**, *197*, 35–46. [CrossRef]

60. Poolwong, J.; Del Gobbo, S.; D'Elia, V. Transesterification of dimethyl carbonate with glycerol by perovskite-based mixed metal oxide nanoparticles for the atom-efficient production of glycerol carbonate. *J. Ind. Eng. Chem.* **2021**, *104*, 43–60. [CrossRef]

61. Rousseau, S.; Loridant, S.; Delichere, P.; Boreave, A.; Deloume, J.P.; Vernoux, P. $La_{(1-x)}Sr_xCo_{1-y}Fe_yO_3$ perovskites prepared by sol–gel method: Characterization and relationships with catalytic properties for total oxidation of toluene. *Appl. Catal. B Environ.* **2009**, *88*, 438–447. [CrossRef]

62. Over, H.; Seitsonen, A.P. Oxidation of metal surfaces. *Science* **2002**, *297*, 2003–2005. [CrossRef]

63. Widmann, D.; Behm, R.J. Active oxygen on a Au/TiO_2 catalyst: Formation, stability, and CO oxidation activity. *Angew. Chem. Int. Ed.* **2011**, *50*, 10241–10245. [CrossRef] [PubMed]

64. Fan, X.H.; Li, L.M.; Yang, X.S.; Guo, Z.L.; Jing, F.L.; Chu, W. High-performance $Co_xM_{3-x}AlO_y$ (M = Ni, Mn) catalysts derived from microwave -assisted synthesis of hydrotalcite precursors for methane catalytic combustion. *Catal. Today* **2020**, *347*, 23–30. [CrossRef]

65. Kessaratikoon, T.; Saengsaen, S.; Del Gobbo, S.; D'Elia, V.; Sooknoi, T. High surface area ZnO-Nanorods catalyze the clean thermal methane oxidation to CO_2. *Catalysts* **2022**, *12*, 1533. [CrossRef]

66. Kucharczyk, B.; Okal, J.; Tylus, W.; Winiarski, J.; Szczygiel, B. The effect of the calcination temperature of $LaFeO_3$ precursors on the properties and catalytic activity of perovskite in methane oxidation. *Ceram. Int.* **2019**, *45*, 2779–2788. [CrossRef]

67. Arandiyan, H.; Dai, H.; Deng, J.; Liu, Y.; Bai, B.; Wang, Y.; Li, X.; Xie, S.; Li, J. Three-dimensionally ordered macroporous $La_{0.6}Sr_{0.4}MnO_3$ with high surface areas: Active catalysts for the combustion of methane. *J. Catal.* **2013**, *307*, 327–339. [CrossRef]

68. An, W.; Baber, A.E.; Fang, X.; Soldemo, M.; Weissenrieder, J.; Stacchiola, D.; Ping, L. Mechanistic study of CO titration on $Cu_xO/Cu(1\,1\,1)$ ($x \leq 2$) surfaces. *ChemCatChem* **2014**, *6*, 2364–2372. [CrossRef]

69. Papaefthimiou, P.; Ioannides, T.; Verykios, X.E. Performance of doped Pt/TiO_2 (W^{6+}) catalysts for combustion of volatile organic compounds (VOCs)-ScienceDirect. *Appl. Catal. B Environ.* **1998**, *15*, 75–92. [CrossRef]

70. Wang, K.; Men, Y.; Liu, S.; Wang, J.G.; Li, Y.Y.; Tang, Y.H.; Li, Z.P.; An, W.; Pan, X.L.; Li, L. Decoupling the size and support/metal loadings effect of Ni/SiO_2 catalysts for CO_2 methanation. *Fuel* **2021**, *304*, 121388. [CrossRef]

71. Li, Y.Y.; Men, Y.; Liu, S.; Wang, J.G.; Wang, K.; Tang, Y.H.; An, W.; Pan, X.L.; Li, L. Remarkably efficient and stable Ni/Y_2O_3 catalysts for CO_2 methanation: Effect of citric acid addition. *Appl. Catal. B Environ.* **2021**, *293*, 120206. [CrossRef]